

PHYSICAL DESIGN CONCEPTS OF VORTEX GENERATOR ARRAYS FOR AIRCRAFT AFT-BODIES DRIVEN BY DISTINCT DRAG REDUCTION MECHANISMS

Yicheng Mou[1], Yiming Wu[1], Tiejun Liu[2], Dongcheng Li[2], Yang Xiang[1] & Hong Liu[1]

[1]School of Aeronautics and Astronautics, Shanghai Jiaotong University, Shanghai 200240, China
[2]COMAC Shanghai Aircraft Design and Research Institute, Shanghai 201210, China

Abstract

Designing vortex generator (VG) arrays for aircraft drag reduction is challenging because of complex aerodynamic interactions and a heavy reliance on trial-and-error methods. This paper presents a physics-based design approach to improve pressure recovery on aft-bodies. Using Detached Eddy Simulations (DES) of the DLR-F6 fuselage, we investigated the unsteady flow physics between VG wakes and large-scale boundary layer separation. Two array setups were tested based on the unforced flow field: a Counter-Rotating Pair (CRP) located at the local vorticity source, and a Co-Rotating Array (CRA) placed along the initial separation line. The findings show two different drag reduction routes. The CRP enhanced fluid mixing and energy dissipation, leading to a quick breakdown of the main vortex. In contrast, the CRA worked as a fluidic fence, using topological partitioning to stop shear-layer merging and keep vortex structures close to the wall. By detailing these distinct mechanisms, this study offers a quantitative framework for arranging VG arrays in flows dominated by large separation vortices.

Keywords: Vortex generators; Drag reduction; Flow control; Aircraft aft-body; Flow separation

1. Introduction

Improving fuel efficiency and lowering emissions are core goals in modern aircraft design, which heavily depend on reducing aerodynamic drag. On aircraft with high-aspect-ratio fuselages, the geometric contraction and upsweep at the rear subject the boundary layer to strong adverse pressure gradients. This often causes three-dimensional flow separation and creates large longitudinal vortices, which drop local pressure and increase drag [1, 2]. To address these flow issues, engineers have widely studied passive flow control devices, especially vortex generators (VGs).

The basic working principle of a single VG is well understood: it creates streamwise vortices that pull high-momentum fluid from the outer flow down into the slower boundary layer, helping to delay or stop flow separation [3]. This method of adding local momentum works well in many applications. For example, Koike et al. [4] showed noticeable drag reduction using standard VGs. For transport aircraft, Buerger et al. [5] proved that micro-vortex generators (MVGs) could reduce aft-body separation, and Herter et al. [6] used sub-boundary-layer devices to change wake structures and improve base pressure. However, a single VG or a few scattered devices only affect a small area. When dealing with the massive separation regions on aircraft aft-bodies, these local fixes usually do not provide the best overall drag reduction.

To control the flow on a larger scale, modern designs often use arrays of vortex generators. Setups like counter-rotating pairs (CRP) and co-rotating arrays (CRA) can reshape the entire wake by forming a continuous “vortex curtain.” However, designing these arrays is aerodynamically complex. The effect of an array is not just the sum of individual vortices. Instead, it involves strong interactions between vortices, such as merging, co-induction, and early breakdown [7]. In the past, placing these

arrays required expensive wind tunnel tests or numerical optimization algorithms that acted like black boxes [8]. These trial-and-error approaches rarely find a clear physical link between the VG layout and the original separation dynamics they aim to fix.

To overcome these issues, the current study developed a physics-based method for designing VG arrays. We used high-fidelity detached eddy simulations (DES) to capture the turbulent structures on the DLR-F6 fuselage [9] and carefully mapped the baseline separation topology. Rather than running blind parametric sweeps, we proposed a direct design link: finding the exact coordinates of the vorticity source and the initial separation line, and using them to position the CRP and CRA configurations, respectively.

This research clarified how CRP and CRA setups alter the aft-body vortex system through different physical routes. By comparing the high-energy wake mixing mechanism with the topological flow partitioning concept, this paper supplies a clear, quantitative guide for designing VG arrays in areas with strong flow separation.

2. Computational Framework and Validation

2.1 Aft-Body Configuration and Free-Stream Conditions

The computational model uses a modified half-span version of the standard DLR-F6 geometry, as shown in Fig. 1(a) [10]. The wing assembly was removed to isolate the aft-body vortex dynamics and save computational resources. This ensures that the VG-induced structures are not mixed with wing downwash or trailing-edge wakes.

Simulations were run under typical transonic cruise conditions. We set the freestream Mach number to $M_\infty = 0.75$ and the Reynolds number to $Re = 1.5 \times 10^6$, based on the maximum fuselage diameter ($D = 148.42$ mm). To check how the aerodynamics respond across normal flight operations, all models were tested at three angles of attack: $\alpha = 0.49^\circ$, 1.6°, and 1.8°.

We used two coordinate systems to map the flow field. The global Cartesian system has its origin at the nose of the fuselage; the x-axis points in the freestream direction, while the y- and z-axes represent the spanwise and vertical directions. The total length of the model is $L = 1188$ mm. For looking at specific cross-sections, we added a cylindrical coordinate system. Its origin is placed at the center of each slice, with the angle (θ) starting at zero on the negative y-axis and moving toward the positive z-axis.

To track how the aft-body vortex develops—from its start, through separation, to its final breakdown—we set up nine evaluation planes. These slices are spaced out along the rear fuselage, covering the streamwise area from $x/L = 0.84$ to 0.98.

2.2 Delayed Detached Eddy Simulation (DDES) Approach

Unsteady flow simulations were carried out using the in-house Navier-Stokes solver *superMan*, which features a parallel overset adaptive mesh refinement (AMR) architecture [11]. Turbulence was modeled with an adaptive Delayed Detached Eddy Simulation (DDES) method based on the Wilcox $k-\omega$ equations [12]. This hybrid solver works well for compressible aerodynamics because it switches to a Large Eddy Simulation (LES) mode near the wall when the grid is fine enough, but acts as standard DDES in coarser areas. This ensures the near-wall turbulence is captured accurately, leading to reliable force and shock wave predictions.

The solver uses a semi-discrete finite volume approach. Spatial fluxes were calculated with a fifth-order Weighted Essentially Non-Oscillatory (WENO) scheme combined with the SLAU2 approximate Riemann solver to keep dissipation low. To track the detached vortices in the wake, a feature-triggered AMR strategy was built into the overset grid system, adding local grid points only where needed. For time stepping, an implicit Lower-Upper Symmetric Gauss-Seidel (LU-SGS) method was applied. This bypasses strict CFL time-step limits, meaning the time steps are driven by the actual physics of the vortex changes rather than acoustic wave speeds [11].

2.3 Domain Definition and Boundary Conditions

To avoid artificial blocking effects and pressure reflections from the boundaries, the calculation domain extends far outward, as shown in Fig. 1(b). The outer boundaries use a Riemann invariant condition set to $M_\infty = 0.75$. Since the fuselage and the VG arrays are symmetric, a symmetry boundary

condition was applied at the $y = 0$ mid-plane. This saves a lot of computing time while still capturing the longitudinal vortex changes accurately. The surfaces of the DLR-F6 and the VGs were set as adiabatic, no-slip walls.

2.4 Adaptive Overset Grid Strategy

The mesh is built with structured hexahedral blocks to capture the different scales of turbulence in the wake. Grid points are clustered inside the boundary layer and along the rear contraction section to catch the exact start of flow separation. To add the CRP and CRA blades without ruining the overall grid quality, each VG blade gets its own high-resolution grid block. Fig. 1(c) shows the detailed body-fitted mesh near the VG. This setup keeps the VG leading and trailing edges sharp, which is essential for predicting the right vortex strength.

To ensure the DDES model works correctly near the solid boundaries, the height of the first grid cell was kept under a non-dimensional wall distance of $y^+ < 1$ everywhere. The unsteady runs started from a converged steady-state result and ran until the flow became statistically stable. Data was then averaged over several convective time scales to ensure the mean flow and vortex behaviors were reliable.

2.5 Solver Validation and Mesh Independence

The aerodynamic performance of the fuselage is measured by the lift (C_l) and drag (C_d) coefficients:

$$C_l = \frac{F_l}{0.5\rho_\infty U_\infty^2 S_{ref}}, \quad C_d = \frac{F_d}{0.5\rho_\infty U_\infty^2 S_{ref}} \tag{1}$$

Because the wing was removed for this study, the reference area S_{ref} is taken as the maximum cross-sectional area of the half-fuselage ($A_{max} = \pi D^2/8$).

Since simulation accuracy depends heavily on the grid, a mesh independence study was conducted using three grid levels (coarse, medium, and fine). Table 1 lists the node distributions and cell counts. All grids maintained $y^+ < 1$ to meet the wall-resolution needs of the DDES model.

Table 1 – Spatial resolution metrics for the grid independence study.

Grid Level	y^+	Streamwise Nodes	Circumferential Nodes	Wall-normal Nodes	Near-body Cells ($\times 10^6$)	Total Cells ($\times 10^6$)
Coarse	< 1	944	145	80	11	57
Medium	< 1	1066	167	90	17	70
Fine	< 1	1188	189	100	22	81

Figure 2 compares the time-averaged total, pressure, and friction drag across the three grids. The coarse grid clearly overpredicted the total drag (around 0.0311), mainly due to a high pressure drag value. As the mesh was refined, the medium and fine grids gave very similar results. The total drag settled at about 0.0301, showing that the fine grid was dense enough to capture the forces correctly. Besides looking at forces, we checked the energy spectrum in the wake behind the VGs to ensure the turbulence was resolving properly. As shown in Fig. 3, the spectrum follows the Kolmogorov $-5/3$ inertial subrange scaling [13]. This means the mesh captures the important turbulent eddies and their energy decay. Based on this, the fine grid was chosen for all the physics analysis that follows.

3. Physics-Driven Array Placement Methodology

3.1 Identification of Separation Zone

For the baseline case at $\alpha = 0.49°$, the adverse pressure gradient from the aft-body contraction resulted in a total drag coefficient of 0.03034. Pressure drag made up about 27.5% of this value. The main cause of this pressure drag is a large 3D flow separation region over the upswept rear fuselage. To find where this drag originates on the wall, we looked at the time-averaged skin friction lines. According to the critical point theory for 3D separated flows [1], separation boundaries appear as distinct patterns in the surface shear stress. The start of separation shows up as a line where surface

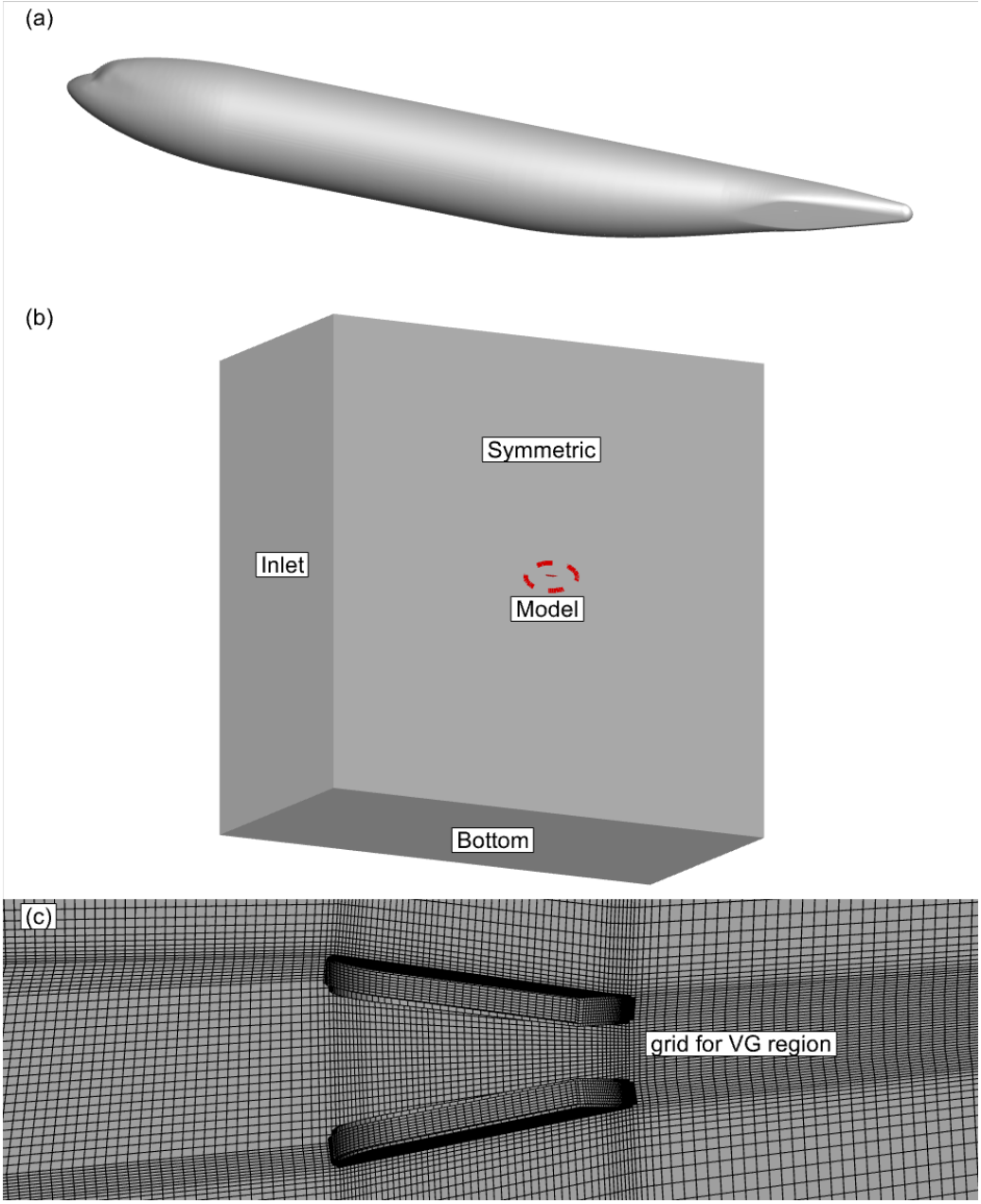


Figure 1 – Overview of the computational setup: (a) the isolated DLR-F6 half-fuselage geometry, (b) the global calculation domain and specified boundary conditions, and (c) the detailed body-fitted structured mesh resolving the vortex generator region.

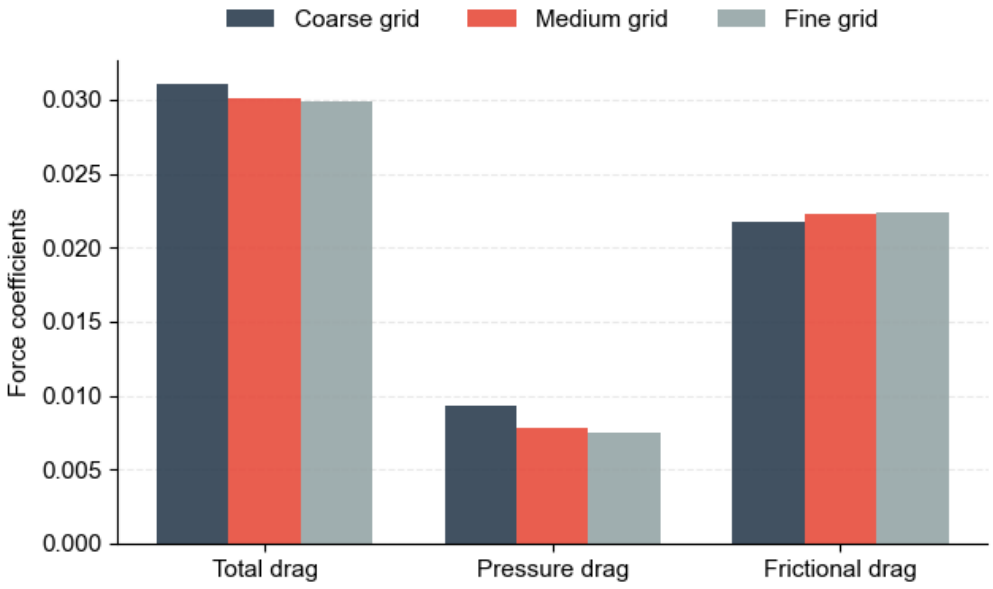


Figure 2 – Comparison of time-averaged aerodynamic force components across three levels of grid refinement.

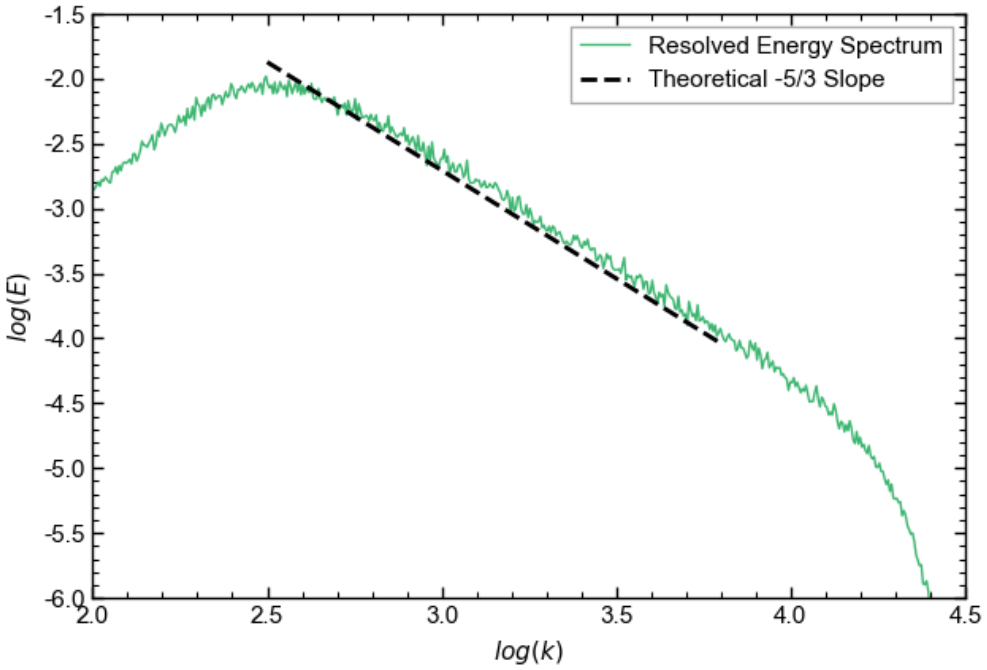


Figure 3 – Turbulent kinetic energy spectrum resolved downstream of the vortex generator, compared with the Kolmogorov $-5/3$ power law.

friction vectors merge together. This primary separation line marks where the main longitudinal vortex lifts off the body. On the other hand, flow reattachment looks like a line where friction vectors spread apart.

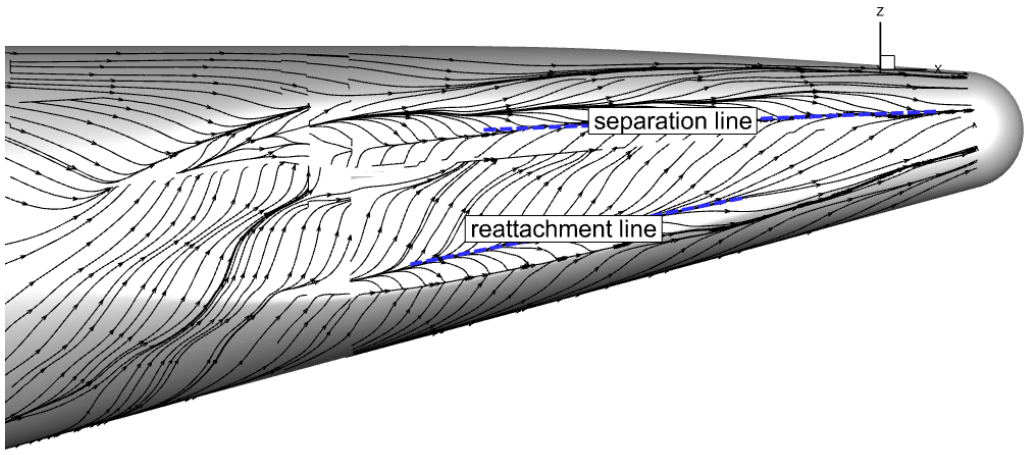


Figure 4 – Time-averaged surface skin friction topology and the topological demarcation of the three-dimensional separation zone on the baseline fuselage ($\alpha = 0.49^\circ$).

The area between these two lines is the vortex-induced separation zone. As seen in Fig. 4, this large separated region started near $x/L = 0.8575$ and grew toward the tail, covering an angle from about -30° to 20°. By stopping the flow from mixing near the wall, this separation zone blocked pressure recovery on the aft-body. Pinpointing these exact boundaries gave us the spatial targets needed for placing the VG arrays.

3.2 Mechanism-Targeted Configuration of CRP and CRA

To make a fair comparison between the two placement strategies, the shape of the VG elements was kept the same for all arrays. Following standard guidelines for sub-boundary-layer devices [8, 4], we used a quasi-trapezoidal shape with a rounded leading edge to keep its own drag low while still generating strong vortices. Fig. 5(a) shows the dimensions: a base length of $l_a = 16$ mm, a top length of $l_b = 10$ mm, and a thickness of $\delta = 1$ mm. Our data showed the local boundary layer thickness (δ_{99}) in this region grew from about 5.3 mm to 9.9 mm. We chose a VG height of $h = 4$ mm, which kept the devices buried within 40% to 75% of the boundary layer—a good range for mixing the slow near-wall fluid [4].

Since the VG shape was fixed, any change in drag had to come from where the arrays were placed. Rather than relying on empirical iteration, we established two distinct placement criteria based on flow physics.

The first rule was for the Co-Rotating Array (CRA). This setup targeted the *initial 3D separation line*. The goal was to place the CRA right next to this line so the co-rotating vortices would act like a fence, blocking the crossflow that usually feeds the main separation vortex.

The second rule was for the Counter-Rotating Pair (CRP). This setup targeted the main *vorticity source*. Based on boundary vorticity flux theory [14], new vorticity is created at the wall mainly by the tangential pressure gradient. By putting the CRP exactly where this circumferential pressure gradient is strongest, the vortex pair should create intense mixing to break up the vorticity production right at the source.

To find these exact spots, we extracted data from the wall. The dimensionless wall shear stress components ($\tau^*_{wx}, \tau^*_{w\theta}, \tau^*_{wr}$) were computed as before. The dimensionless surface pressure gradient vector, ∇p^*, was calculated using the static pressure field p:

$$\nabla p^*_x = \frac{L}{\rho_\infty a^2_\infty}\frac{\partial p}{\partial x}, \quad \nabla p^*_\theta = \frac{L}{\rho_\infty a^2_\infty r}\frac{\partial p}{\partial \theta}, \quad \nabla p^*_r = \frac{L}{\rho_\infty a^2_\infty}\frac{\partial p}{\partial r} \tag{2}$$

Figure 6 shows these values plotted around the circumference at two key locations. At $x/L = 0.8575$ (Fig. 6a), the circumferential wall shear stress ($\tau^*_{w\theta}$) crossed zero exactly at $\theta = 19.2^\circ$ (Position A).

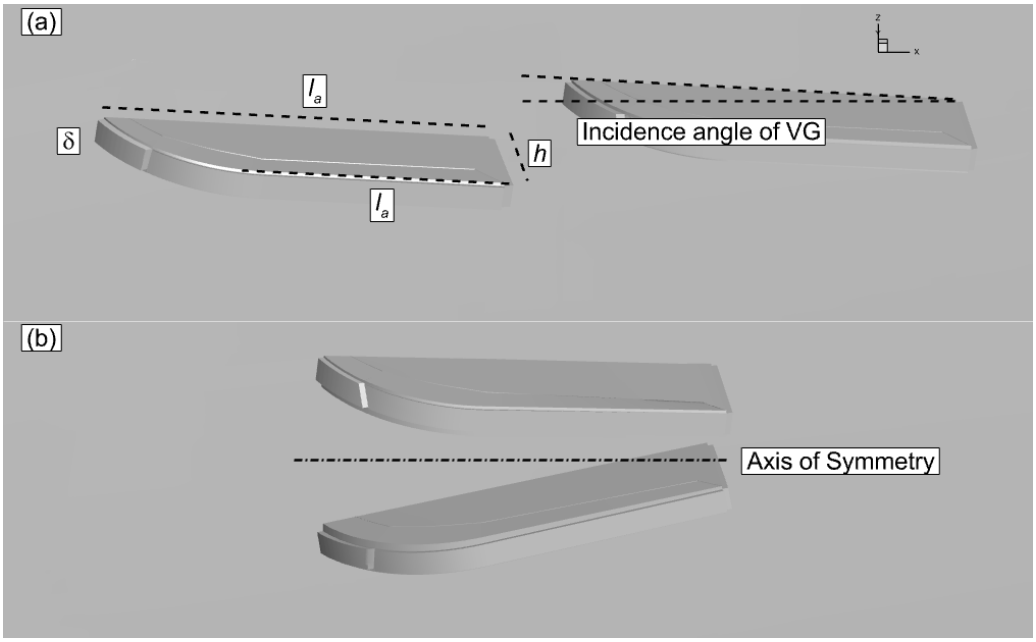


Figure 5 – Geometric parameters and orientation definitions of the vortex generator arrays: (a) profile definition and parameters, illustrated using the CRA configuration; (b) schematic of the longitudinal symmetric placement for the CRP configuration.

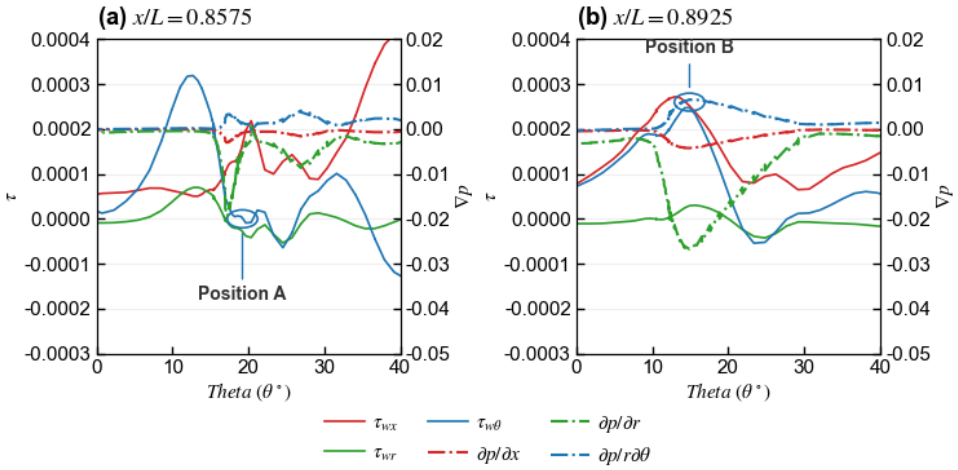


Figure 6 – Circumferential distributions of the dimensionless wall shear stress and surface pressure gradient at two critical streamwise stations: (a) $x/L = 0.8575$, and (b) $x/L = 0.8925$.

This zero-crossing marks the physical start of the primary separation line. Therefore, the front blade of the CRA was placed exactly at Position A. Further downstream at $x/L = 0.8925$ (Fig. 6b), the circumferential pressure gradient (∇p^*_θ) hit a distinct peak at $\theta = 14.9^\circ$ (Position B). Thus, the front blade of the CRP was placed at Position B to target the vorticity source.
Different installation angles were used to get the best vortex strength for each task. For the CRA, both blades were set at an absolute angle (AOA_{abs}) of 9°, giving them a relative angle (AOA_{local}) of 4.5° against the local flow. For the CRP, an asymmetric setup was used (Fig. 5b). The top blade was set to $\text{AOA}_{abs} = 7.5^\circ$ ($\text{AOA}_{local} = 3^\circ$), and the bottom blade was mirrored across the streamline to create the counter-rotating pair. All geometry and location parameters are listed in Table 2.

Table 2 – Key aerodynamic and geometric design parameters of the CRA and CRP configurations.

Category	Parameter	CRA	CRP	Physical Rationale
Placement†	x/L	0.8575	0.8925	Evaluated via surface topology
	θ	19.2°	14.9°	Alignment with separation / source
Orientation	AOA_{local}	4.5°	3° (Upper) / Sym. (Lower)	Baseline local streamline angle
	AOA_{abs}	9°	7.5° (Upper) / Sym. (Lower)	Prescribed installation incidence
Geometry	l_a (mm)	16	16	
	l_b (mm)	10	10	Empirically optimized for
	h (mm)	4	4	sub-boundary-layer control
	δ (mm)	1	1	

† Positional coordinates (x/L, θ) designate the leading edge of the foremost blade.

4. Comparative Aerodynamic Evaluation and Mechanism Elucidation

4.1 Quantification of Drag Components and Overall Performance

We evaluated the integrated force coefficients for the baseline (BF), CRA, and CRP configurations at a cruise incidence of $\alpha = 0.49^\circ$ to see the aerodynamic benefits. The total drag (C_d) was broken down into pressure (C_{dp}) and friction (C_{df}) to pinpoint why the performance changed. Table 3 lists the results.

Table 3 – Aerodynamic force coefficients and relative variations compared to the baseline fuselage ($\alpha = 0.49^\circ$).

Configuration	C_d	C_{dp}	C_{df}	ΔC_d (%)	ΔC_{dp} (%)	ΔC_{df} (%)
BF	0.03034	0.00834	0.02200	—	—	—
CRA	0.02896	0.00698	0.02198	-4.55	-16.3	≈ 0.0
CRP	0.02995	0.00794	0.02201	-1.29	-4.8	$+0.05$

The CRA setup, placed at the initial separation line, provided better aerodynamic control. It reduced the total drag coefficient to 0.02896, a 4.55% drop from the baseline. This improvement came almost entirely from a large drop in pressure drag, which fell by 16.3% (C_{dp} went from 0.00834 down to 0.00698). Interestingly, the usual friction penalty that comes with VGs did not occur here [8]; the friction coefficient barely changed ($C_{df} = 0.02198$). This suggests that the flow barrier created by the CRA reduced the main separation region without adding extra skin friction downstream.
On the other hand, the CRP configuration placed at the vorticity source provided a smaller total drag reduction of 1.29% ($C_d = 0.02995$). It managed to lower the pressure drag by 4.8%, but the strong mixing from the counter-rotating vortices added a slight friction penalty (C_{df} went up to 0.02201). While both methods worked to recover some base pressure, building a topological barrier with the CRA was clearly more efficient for this large-scale separation than the forced mixing approach of the CRP.

4.2 Enhancement of Aft-Body Pressure Recovery

To physically back up the pressure drag changes seen in Table 3, we looked at the time-averaged dimensionless surface pressure (p^*) over the rear fuselage. This value is normalized using freestream conditions:

$$p^* = \frac{p}{\rho_\infty a_\infty^2} \tag{3}$$

Figure 7 compares the pressure maps for the three cases at $\alpha = 0.49°$.

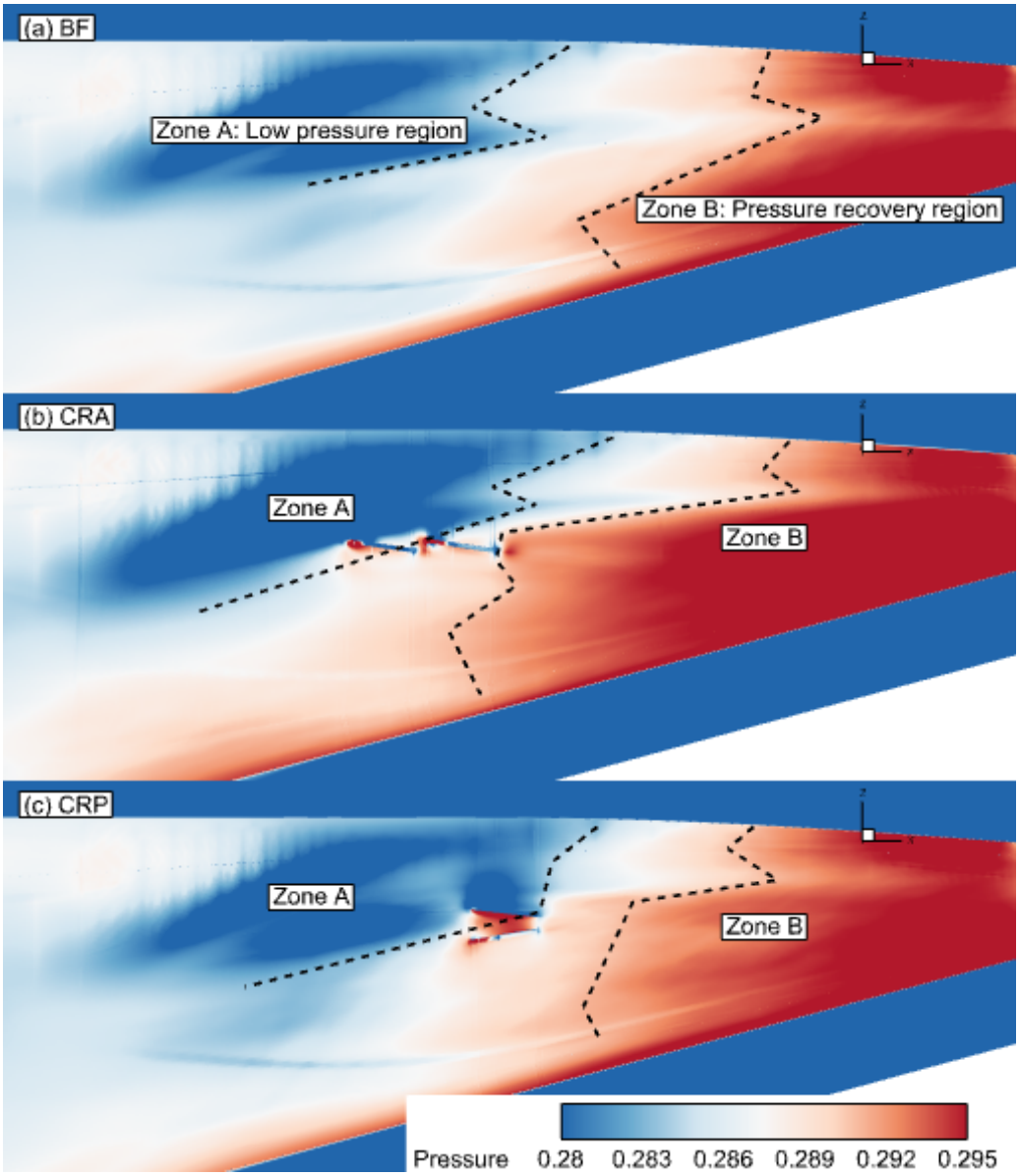


Figure 7 – Time-averaged dimensionless surface pressure distributions over the aft-body contraction region: (a) Baseline Fuselage (BF), (b) CRA configuration, and (c) CRP configuration. Contours illustrate the notable expansion of the terminal pressure recovery zone under CRA control.

For the baseline fuselage (Fig. 7a), the upward curve of the tail caused the boundary layer to detach early, leaving a large, low-pressure suction zone over the middle-to-rear section. Because of this, the high-pressure recovery area at the very end of the tail was very small. This failure to recover base pressure is the main reason the bare fuselage has such high pressure drag [15].
Adding the CRA (Fig. 7b) changed the pressure layout significantly. The co-rotating vortices sped up the fluid near the wall, which caused a small low-pressure penalty just above and behind the VGs. However, this small loss was easily offset by a much larger high-pressure recovery zone at the tail. By acting like a fence that held back the main separation, the CRA kept the flow partially attached further

downstream, allowing the dynamic pressure to turn back into static pressure over a larger area. This visualization is highly consistent with the 16.3% reduction in pressure drag quantified previously.
The CRP configuration (Fig. 7c) created a different footprint. Although its vortices mixed the flow enough to improve pressure recovery compared to the baseline, the high-pressure zone at the tail was noticeably smaller and weaker than with the CRA. The forced mixing approach worked locally near the VGs, but it could not reshape the entire wake as effectively as the CRA's flow-partitioning method.

4.3 Spatial Dynamics and Energetics of the Controlled Wake

4.3.1 Kinematic Evolution of the Longitudinal Vortex System

To explain how the different setups achieved pressure recovery, we tracked the time-averaged longitudinal vorticity field as it moved downstream. The dimensionless axial vorticity is calculated as:

$$\omega_x^* = \frac{\omega_x L}{a_\infty} \tag{4}$$

Figure 8 shows these vorticity slices at four locations ($x/L = 0.900$ to 0.975) for all three test cases.

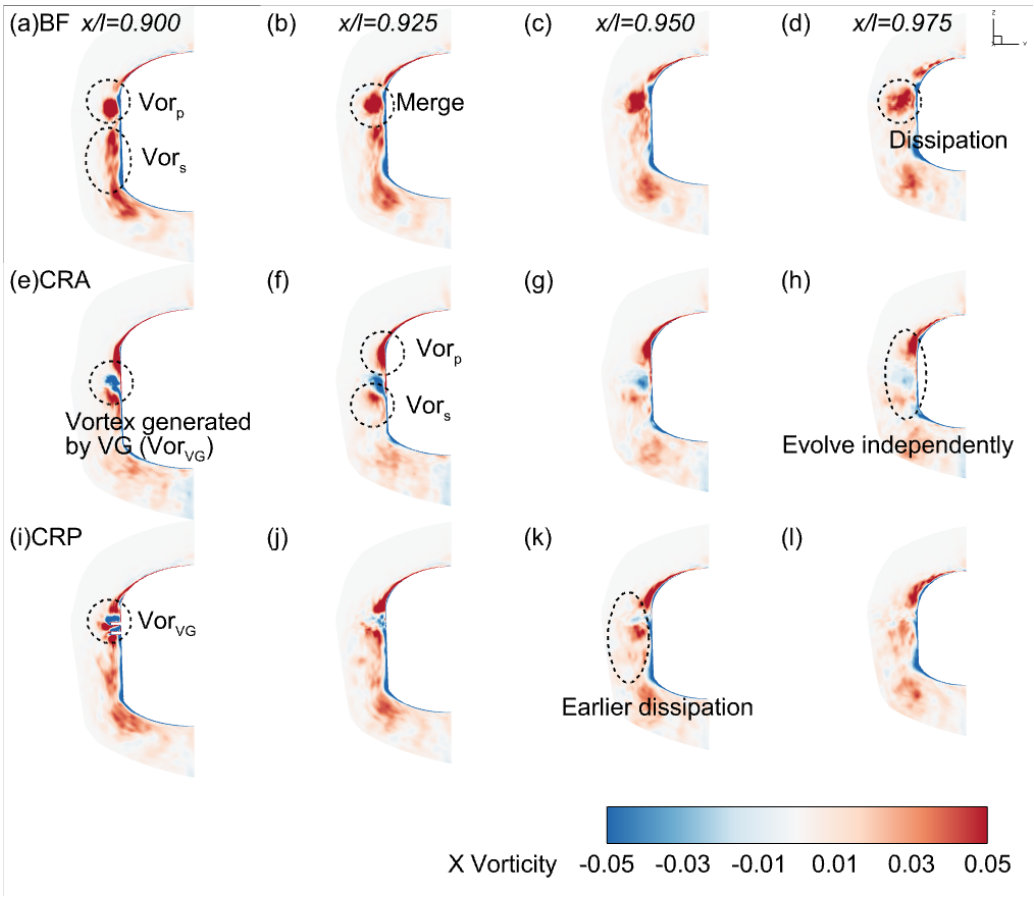


Figure 8 – Spatial evolution of the time-averaged dimensionless longitudinal vorticity fields (ω_x^*) across four successive aft-body cross-sections ($x/L = 0.900$ to 0.975). The rows represent the Baseline Fuselage (BF), CRA, and CRP configurations, respectively.

In the baseline case (Fig. 8, top row), separation started with positive vorticity (Vor$_s$) building up near the inner wall, while the shear layer above it rolled into the main streamwise vortex (Vor$_p$). By $x/L = 0.925$, the main vortex actively pulled in the near-wall Vor$_s$, combining into a single large structure. At $x/L = 0.950$, this main vortex separated from the shear layer and lifted off the surface. Without its energy source, the vortex eventually broke down further downstream. This lift-off and growing vortex size are what caused the large low-pressure area seen earlier on the body surface.
When the CRA was placed at the separation line (Fig. 8, middle row), it worked like a fluidic wall. The array generated a row of co-rotating vortices (Vor$_{VG}$) that physically split the boundary layer.

This prevented the crossflow from merging Vor_p and Vor_s together. Forced to stay separate, the vortex structures remained as small, discrete entities instead of coalescing into a single massive wake structure. Also, the downwash from the CRA kept Vor_p pinned closer to the fuselage. In classic aerodynamic theory [16], keeping the low-pressure wake small is the key to maximizing pressure recovery. By holding the vortices tight against the wall and stopping lift-off, the CRA turned this blocking effect into excellent drag reduction.

The CRP, placed at the vorticity source (Fig. 8, bottom row), worked through energy dissipation instead. It sent a counter-rotating vortex pair (Vor_{VG}) straight into the core of the main vortex. Rather than stopping the merge, this setup forced a heavy mixing process that made the vortex core unstable. The strong interaction deformed Vor_p quickly, making it break down much earlier than in the baseline flow. While breaking up the wake did help recover some base pressure, it failed to stop the initial separation area from growing. This is why the CRP was less aerodynamically efficient than the CRA's barrier approach.

4.3.2 Turbulent Fluctuation Intensity and Wake Dissipation

While the vorticity slices show how the wake moved, looking at the turbulent kinetic energy (TKE) reveals where energy was lost. TKE measures the intensity of the velocity fluctuations and is defined as:

$$\text{TKE}^* = \frac{\overline{u'u'} + \overline{v'v'} + \overline{w'w'}}{2U_\infty^2} \tag{5}$$

where u', v', and w' are the velocity fluctuations in the three directions, and the overbar means time-averaged. Higher TKE values generally indicate stronger momentum transport, vortex stretching, and turbulent dissipation [13]. Figure 9 maps the TKE at the same four cross-sections.

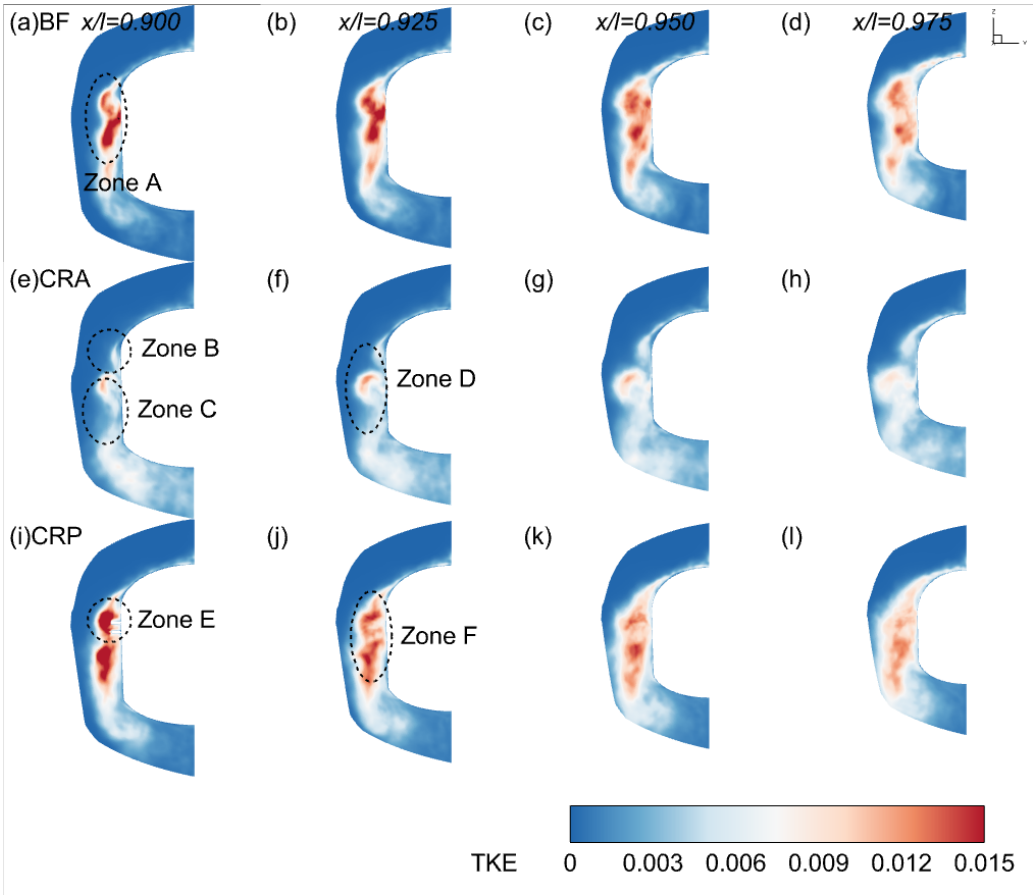


Figure 9 – Spatial evolution of the dimensionless resolved turbulent kinetic energy (TKE) fields across four successive aft-body cross-sections ($x/L = 0.900$ to 0.975). The rows represent the Baseline Fuselage (BF), CRA, and CRP configurations, respectively.

For the baseline fuselage (Fig. 9, top row), the areas of high TKE matched up exactly with the main separated vortex and the shear layer feeding it. As the vortex lifted off and broke down, the fluctuation energy spread over a wide area at the tail, meaning energy was being lost to the wake in a disorganized way.
With the CRA (Fig. 9, middle row), both the peak TKE value and the size of the TKE region dropped noticeably. Because the CRA created a barrier that stopped the shear layer from merging and kept the vortices near the wall, it physically blocked large velocity fluctuations. This lower TKE reading confirmed that the CRA reduced energy waste in the aft-body flow. In aerodynamics, reducing wake dissipation means lowering parasite drag [17], which perfectly lines up with the CRA's strong drag reduction numbers.
The CRP configuration (Fig. 9, bottom row) showed a completely different energy pattern. By targeting the vorticity source to force mixing, the CRP created a large increase in TKE. The intense interaction between the VG vortices and the primary separation structure caused strong velocity fluctuations, generating an elevated TKE peak that persisted and expanded downstream. This high-TKE footprint confirms the energetic dissipation mechanism of the CRP: it achieved base pressure recovery by aggressively breaking down the wake's coherence through intense turbulent mixing. However, the substantial energy penalty associated with this turbulence production explains why its overall drag reduction was lower than the CRA's more aerodynamically efficient approach.

4.3.3 Topological Confinement of the Surface Separation Zone

Lastly, we checked how these 3D flow mechanisms affected the footprint on the physical surface. Figure 10 shows the mean surface flow lines. To make comparison easier, the main separation and reattachment lines from the baseline case are drawn as red dashed lines over the new results.

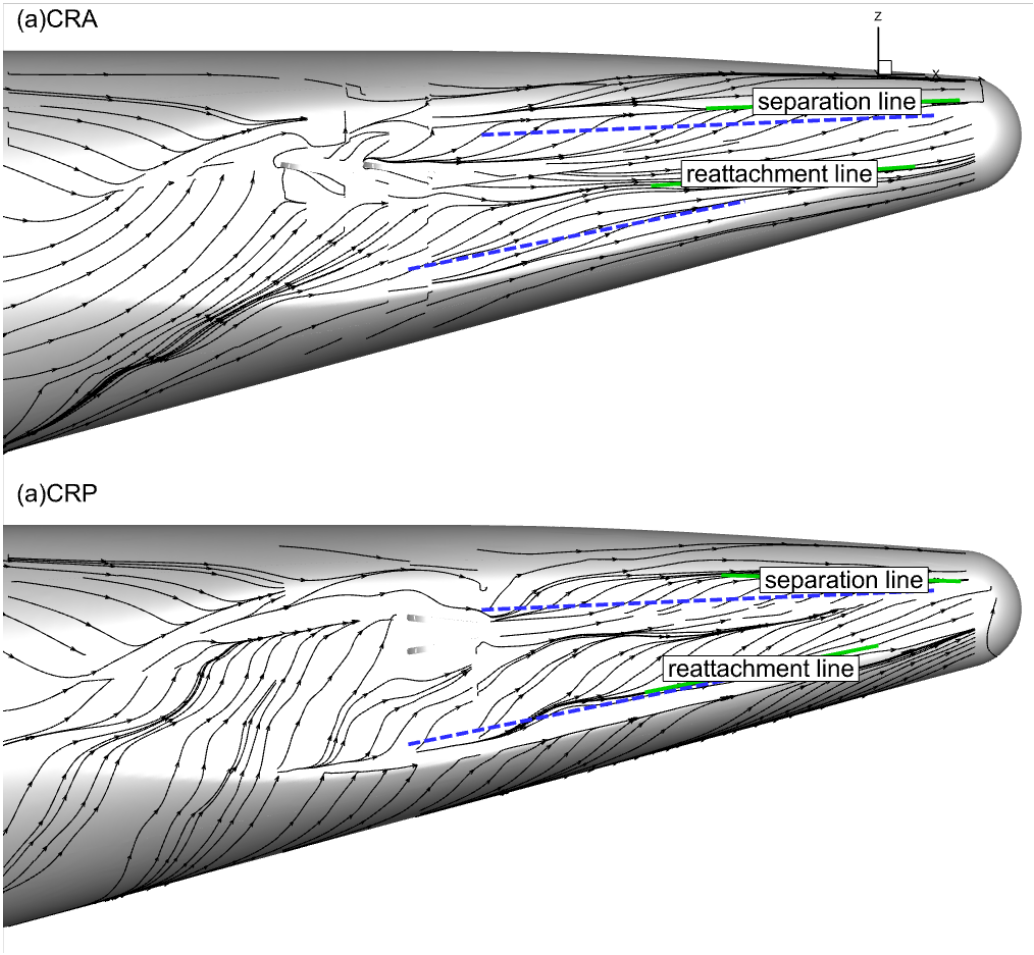


Figure 10 – Time-averaged surface skin friction topology under active control: (a) CRA configuration, and (b) CRP configuration. The primary separation and reattachment lines of the baseline fuselage are superimposed as red dashed lines for direct comparison.

As seen in Fig. 10(a), the CRA changed the separation footprint fundamentally. It did not significantly delay the longitudinal onset of separation; instead, the co-rotating vortices acted like a continuous fluidic barrier that squeezed the separation zone inward from the sides. This lateral narrowing on the surface proves the flow partitioning effect, showing how the CRA stopped the separation from growing wider. According to standard aerodynamic guidelines [16], keeping the separation wake as small as possible is the primary way to improve base pressure. Squeezing the separation zone is exactly how the CRA achieved its superior drag reduction.

The CRP (Fig. 10b) altered the surface topology in a different way. It did not squeeze the separation zone from the sides like the CRA did. Instead, the strong mixing from the counter-rotating vortices delayed the start of the primary separation line, pushing the separation further back toward the tail. While this shorter separation zone was enough to recover some base pressure and reduce drag, the CRP failed to stop the separation from spreading laterally. This wider footprint matches the higher energy losses (TKE) seen earlier, explaining its lower efficiency compared to the CRA. Overall, both arrays reduced drag by changing the boundary layer separation, but they did so using entirely different methods.

5. Concluding Remarks

This study developed a physics-based design approach for VG arrays aimed at reducing large-scale 3D flow separation on aircraft aft-bodies. High-fidelity DES on the DLR-F6 fuselage allowed us to extract the exact locations of the initial separation line and the main vorticity source from the baseline flow. These locations guided the placement of a Co-Rotating Array (CRA) and a Counter-Rotating Pair (CRP).

The CRA, serving as a fluidic barrier at the initial separation line, provided the best aerodynamic performance, reducing total drag by 4.55% and pressure drag by 16.3%. This setup stopped crossflow from merging the shear layer with the primary vortex. By holding the vortex structures close to the wall, the CRA squeezed the surface separation zone inward from the sides. It also suppressed velocity fluctuations, lowering turbulent kinetic energy (TKE) dissipation. This led to better base pressure recovery without adding extra friction drag.

The CRP, placed at the peak of vorticity production, worked through energy dissipation instead. By forcing strong mixing, the counter-rotating vortices destabilized the main vortex core and caused it to break down early. This interaction successfully delayed the start of separation along the length of the body, yielding a 1.29% reduction in total drag. However, it also caused a clear increase in TKE, representing a drag penalty from the heavy turbulent mixing. Because it could not stop the separation zone from widening laterally, it proved less aerodynamically efficient than the CRA.

By moving away from trial-and-error VG placement and focusing on the underlying mechanisms, this research clarifies the differences between topological flow blocking and energetic wake mixing. This provides a clear, quantitative guide for optimizing VG arrays on aircraft aft-bodies.

6. Contact Author Email Address

Yang Xiang: xiangyang@sjtu.edu.cn

7. Copyright Statement

The authors confirm that they, and/or their company or organization, hold copyright on all of the original material included in this paper. The authors also confirm that they have obtained permission, from the copyright holder of any third party material included in this paper, to publish it as part of their paper. The authors confirm that they give permission, or have obtained permission from the copyright holder of this paper, for the publication and distribution of this paper as part of the ICAS proceedings or as individual off-prints from the proceedings.

References

[1] M. Tobak and D. J. Peake. Topology of three-dimensional separated flows. *Annual Review of Fluid Mechanics*, 14(1):61–85, 1982.

[2] M. J. Lighthill. Attachment and separation in three-dimensional flow. In L. Rosenhead, editor, *Laminar boundary layers*, pages 72–82. Clarendon Press, Oxford, 1963.

[3] H. Schlichting and J. Kestin. *Boundary-layer theory*. McGraw-Hill, New York, 1990.

[4] M. Koike, T. Nagayoshi, and N. Hamamoto. Research on aerodynamic drag reduction by vortex generators. *Mitsubishi Motors Technical Review*, 16:11–16, 2004.

[5] C. Buerger, C. Lisy, F. Thiele, et al. Aerodynamic drag reduction of transport aircraft by micro vortex generators. In *27th International Congress of the Aeronautical Sciences (ICAS)*, Nice, France, 2010.

[6] C. Herter, P. Scholz, and R. Radespiel. Experimental investigation of sub-boundary layer vortex generators on a transport aircraft configuration. *CEAS Aeronautical Journal*, 10(2):489–501, 2019.

[7] G. Godard and M. Stanislas. Control of a decelerated turbulent boundary layer using micro-vortex generators. *Aerospace Science and Technology*, 10(3):181–191, 2006.

[8] J. C. Lin. Review of low-profile vortex generators to control boundary-layer separation. *Progress in Aerospace Sciences*, 38(4-5):389–420, 2002.

[9] P. Sagaut, M. Terracol, and S. Deck. *Multiscale and multiresolution approaches in turbulence: LES, DES and Hybrid RANS/LES Methods*. World Scientific, Singapore, 2013.

[10] J. C. Vassberg, E. N. Tinoco, M. Mani, O. P. Brodersen, B. Eisfeld, R. A. Wahls, J. H. Morrison, T. Zickuhr, D. W. Levy, and D. J. Mavriplis. Summary of the third aiaa computational fluid dynamics drag prediction workshop. *Journal of Aircraft*, 45(3):781–798, 2008.

[11] G. Li, X. Fu, and F. Wang. High-resolution multi-code implementation of unsteady Navier–Stokes flow solver based on paralleled overset adaptive mesh refinement and high-order low-dissipation hybrid schemes. *International Journal of Computational Fluid Dynamics*, 31(9):379–395, 2017.

[12] Zifei Yin and Paul A. Durbin. An adaptive DES model that allows wall-resolved eddy simulation. *International Journal of Heat and Fluid Flow*, 62:499–509, 2016.

[13] S. B. Pope. *Turbulent flows*. Cambridge University Press, Cambridge, 2000.

[14] J. Z. Wu, X. Y. Lu, A. G. Denny, M. Fan, and J. M. Wu. Post-stall flow control on an airfoil by local unsteady forcing. *Journal of Fluid Mechanics*, 371:21–58, 1998.

[15] T. Morel. Effect of base slant on flow in the near wake of an axisymmetric cylinder. *Aeronautical Quarterly*, 31(2):132–147, 1980.

[16] S. F. Hoerner. *Fluid-Dynamic Drag: Practical Information on Aerodynamic Drag and Hydrodynamic Resistance*. Hoerner Fluid Dynamics, Bakersfield, CA, 1965.

[17] K. Oswatitsch. Der luftwiderstand als integral des entropiestromes. *Nachrichten der Akademie der Wissenschaften in Göttingen, Mathematisch-Physikalische Klasse*, 1:88–90, 1956.